ACS NANO

www.acsnano.org

ARTICLE

Enhancing Hydrogen Evolution Reaction Activity of Palladium Catalyst by Immobilization on MXene Nanosheets

Yiyang Sun, Jihyeong Lee, Nam Hee Kwon, Joohyun Lim, Xiaoyan Jin,* Yury Gogotsi,* and Seong-Ju Hwang*

Cite This: *ACS Nano* 2024, 18, 6243−6255

Read Online

ACCESS | Metrics & More | Article Recommendations | Supporting Information

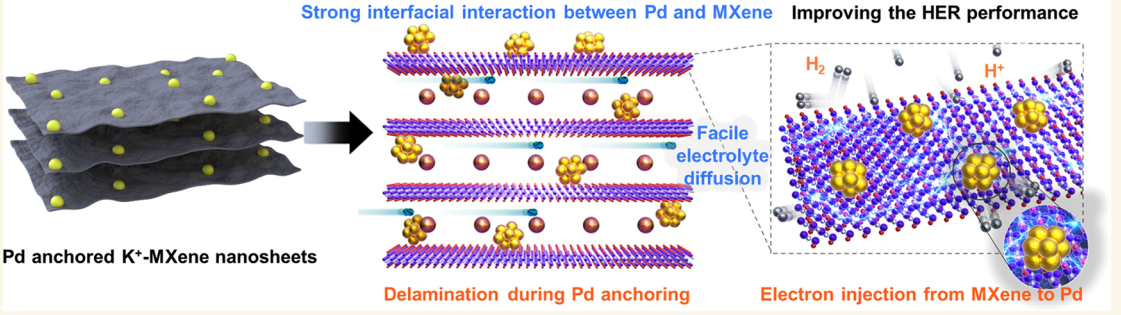

ABSTRACT: **Efficient catalysts with minimal content of catalytically active noble metals are essential for the transition to the clean hydrogen economy. Catalyst supports that can immobilize and stabilize catalytic nanoparticles and facilitate the supply of electrons and reactants to the catalysts are needed. Being hydrophilic and more conductive compared with carbons, MXenes have shown promise as catalyst supports. However, the controlled assembly of their 2D sheets creates a challenge. This study established a lattice engineering approach to regulate the assembly of exfoliated $Ti_3C_2T_x$ MXene nanosheets with guest cations of various sizes. The enlargement of guest cations led to a decreased interlayer interaction of MXene lamellae and increased surface accessibility, allowing intercalation of Pd nanoparticles. Stabilization of Pd nanoparticles between interlayer-expanded MXene nanosheets improved their electrocatalytic activity. The Pd-immobilized K^+-intercalated MXene nanosheets (PdKMX) demonstrated exceptional electrocatalytic performance for the hydrogen evolution reaction with the lowest overpotential of 72 mV (@10 mA cm^{-2}) and the highest turnover frequency of 1.122 s^{-1} (@ an overpotential of 100 mV), which were superior to those of the state-of-the-art Pd nanoparticle-based electrocatalysts. Weakening of the interlayer interaction during self-assembly with K^+ ions led to fewer layers in lamellae and expansion of the MXene in the *c* direction during Pd anchoring, providing numerous surface-active sites and promoting mass transport. *In situ* spectroscopic analysis suggests that the effective interfacial electron injection from the Pd nanoparticles strongly immobilized on interlayer-expanded PdKMX may be responsible for the improved electrocatalytic performance.**

KEYWORDS: *MXene, interfacial electronic coupling, electrocatalyst, hydrogen evolution reaction (HER), 2D materials*

Two-dimensional (2D) MXenes have attracted significant attention as promising candidates for applications in electrodes, electrocatalysts, and hybridization matrices due to their exceptional electrical conductivity, high electrochemical activity, and diverse structures and chemical compositions.[1,2] These properties and abundant surface functional groups of MXenes make them attractive as immobilization matrices for nanoparticles.[3,4] Considering that preventing restacking of inorganic nanosheets can improve the surface reactivity,[5] the regulation of 2D materials assembly to create porous architectures presents a valuable opportunity to anchor nanoparticles and enhance their interaction with MXene nanosheets.[6,7] Besides, the assembly of 2D nanosheets,

Received: October 5, 2023
Revised: February 3, 2024
Accepted: February 6, 2024
Published: February 12, 2024

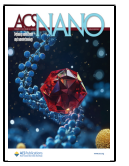

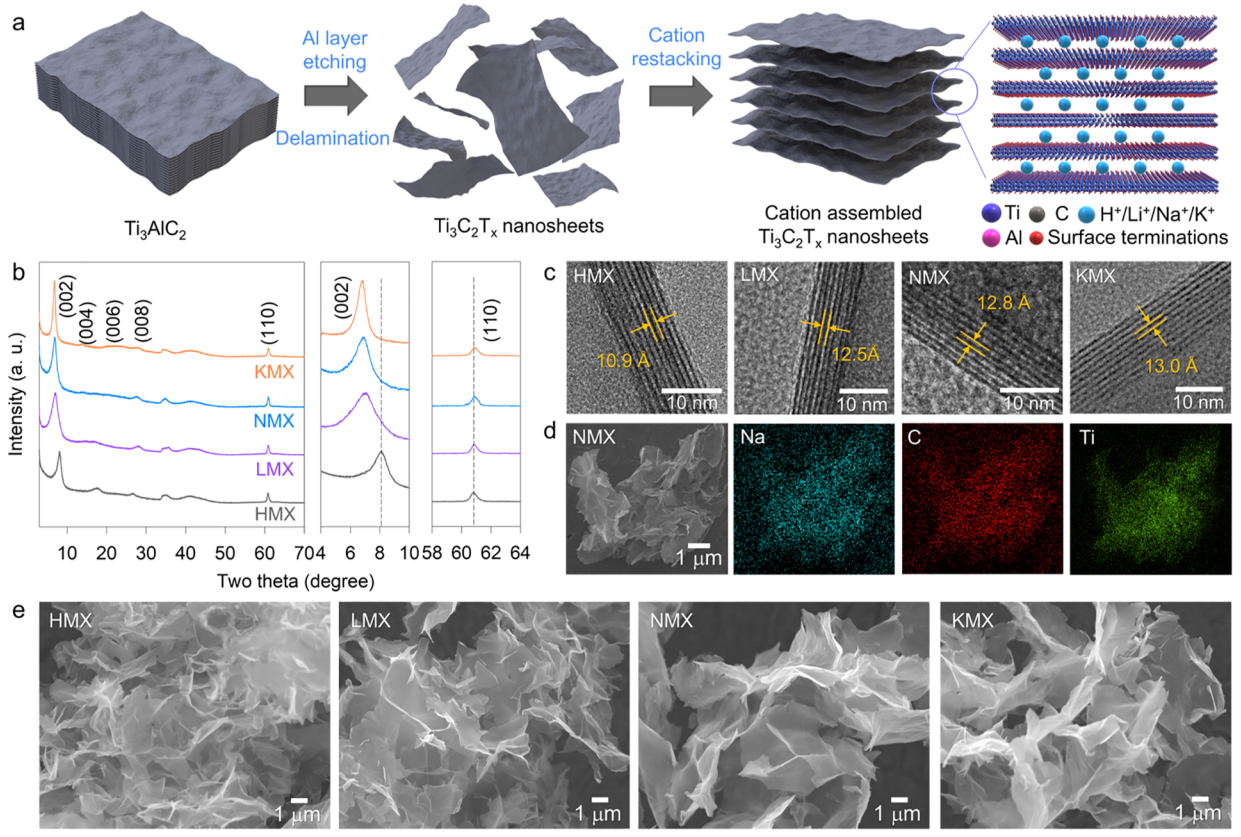

Figure 1. (a) Exfoliation-assembly route to control the stacking and assembled architectures of MXene. (b) Powder XRD, (c) TEM, (d) EDS elemental maps, and (e) FE-SEM images of assembled MXene architectures.

including the interlayer distance and the number of monolayers, profoundly affects their efficiency as immobilization matrices for anchoring metal nanoparticles.[8−10] In particular, the incorporation of nanoparticles into the interlayer space is supposed to enhance the interfacial electronic coupling with MXene nanosheets through intimate contact at nanoscale. Therefore, simultaneous control of stacking and assembling MXene nanosheets into open architectures is necessary for maximizing the impact of hybridization on the functionality of confined catalytic species.[11,12] Considering the decrease in the lattice energy observed in intercalated layered solids due to increased interlayer distance,[13,14] a basal plane expansion during assembling with bulky species is expected to increase misalignment of ultrathin exfoliated MXene nanosheets. Moreover, the alteration in the charge density of the guest species can effectively tune the electrostatic interaction with MXene and control the assembly of nanosheets. Consequently, self-assembly with various guest cations of different sizes and charge densities has been proposed as an effective method to simultaneously tailor the surface reactivity and structural disorder and assemble 2D MXenes into a desired shape. Despite the extensive research conducted on MXene materials,[15,16] there are no previous reports on the simultaneous control of the stacking and surface accessibility in exfoliated MXene nanosheets for intercalating metal nanoparticles between MXene layers to explore high-performance catalysts.

This study presents a soft chemical lattice engineering approach to simultaneously tailor the packing and assembly of 2D MXene nanosheets with guest cations of varying sizes. We systematically investigated the impact of guest types on the surface accessibility and structural order of the exfoliated MXene nanosheets to gain insight into the evolution of their chemical bonding characteristics and functionality. Furthermore, we used the assembled MXene sheets with controlled surface accessibility and lamellae thickness as an immobilization matrix for intercalating Pd nanoparticles to enhance their electrocatalytic performance for hydrogen evolution reaction (HER).

RESULTS AND DISCUSSION

Figure 1a illustrates the exfoliation of the pristine MAX phase (i.e., Ti_3AlC_2) into single-layer MXene (i.e., $Ti_3C_2T_x$). This exfoliation was achieved through selective etching of the Al layers from the precursor using a mixture of hydrochloric and hydrofluoric acids and overcoming the van der Waals forces between the formed MXene sheets by intercalating metal ions.[17] The formation of monolayer MXene was verified through atomic force microscopy (AFM). Figure S1a demonstrates a highly anisotropic 2D morphology, with single-layer flakes having a thickness of ∼1.4 nm (MXene sheet plus adsorbed water) and lateral dimensions at the micrometer scale. Transmission electron microscopy (TEM) further confirmed the formation of ultrathin MXene nanosheets (Figure S1b). Zeta potential measurements (Figure S1c) indicated the anionic nature of the exfoliated MXene nanosheets, with a highly negative potential of −61 mV. Due to the negative surface charge of exfoliated MXene nanosheets, various guest cations could be assembled with negatively charged MXene nanosheets in terms of electrostatic interaction, resulting in the flocculation of colloidal MXene nanosheets. Various alkali metal cations (Li^+, Na^+, and K^+)

https://doi.org/10.1021/acsnano.3c09640
ACS Nano 2024, 18, 6243−6255

and protons (H^+) were used as guest species to assemble exfoliated MXene nanosheets and investigate the impact of the guest species on the restacking and assembled architectures (see Figure 1a). To initiate the assembly of exfoliated MXene nanosheets, an excess of guest ions was added to the suspension of colloidal MXene nanosheets. The precipitates with Li^+, Na^+, K^+, and H^+ materials were designated as LMX, NMX, KMX, and HMX, respectively.

The powder X-ray diffraction (XRD) patterns shown in Figure 1b revealed distinct (*00l*) reflections in the low-angle region for the assembled MXene nanosheets with guest cations. These reflections indicate the formation of a layer-by-layer periodic intercalation structure with an expanded interlayer spacing. The shift of (*00l*) reflections toward lower angles with the enlargement of guest cations distinctly demonstrated an increase in the interlayer distance in the following order: HMX < LMX < NMX < KMX (see Tables 1 and S1). It was previously shown that solvated K^+ stays at a larger distance from the MXene surface and has weaker interaction with the surface compared to solvated Li^+, Na^+, and H^+ ions.[18] Except for HMX, all MXene materials assembled with alkali metal ions exhibited progressively sharpened (*00l*) reflections with increasing alkali metal size, suggesting a gradual increase in stacking thickness and improved periodicity for the MXene nanosheets, as supported by Scherrer's calculations (Table 1), even though those have limited applicability to 2D materials, as other factors, such as bending of 2D sheets, can affect the results. Besides the (*00l*) reflections, all assembled MXene materials with a random orientation of flakes maintained the in-plane (*110*) peak, validating the preservation of the in-plane structure of the MXene lattice.[19] This peak showed a gradual increase of full-width-at-half-maximum (fwhm) with increasing guest size, indicating increased misalignment between MXene sheets. Such an increase in the interlayer spacing and misalignment of MXene sheets can facilitate electrolyte penetration and reduce the diffusion distance of the ions.[20]

Table 1. *d*-Spacing, Layer Thickness, and Stacking Number of Assembled MXene Nanosheets

Material	*d*-spacing (nm)	Layer thickness (nm)	Stacking number
HMX	1.10 (±0.03)	10.9 (±0.2)	10
LMX	1.25 (±0.08)	9.1 (±1.7)	7
NMX	1.28 (±0.04)	10.1 (±0.3)	8
KMX	1.30 (±0.03)	12.6 (±0.4)	10

The controllability of the *d*-spacing distance and lamella thickness of the assembled MXene nanosheets was confirmed through TEM (Figure 1c). The distribution plots of the lamellae thickness (Figure S2) supported the observation that an increase in alkali metal ions led to the thickening of the assembled MXene lamellae, consistent with the XRD results. Considering the role of the hydration shell as a dielectric layer that suppresses the electrostatic interaction with anionic MXene nanosheets, the observed thickening of the assembled MXene lamellae in the order of LMX < NMX < KMX could be understood as a consequence of the thinning of the hydration layers (Table S1) and the resulting enhanced electrostatic interactions between the host and guest during the self-

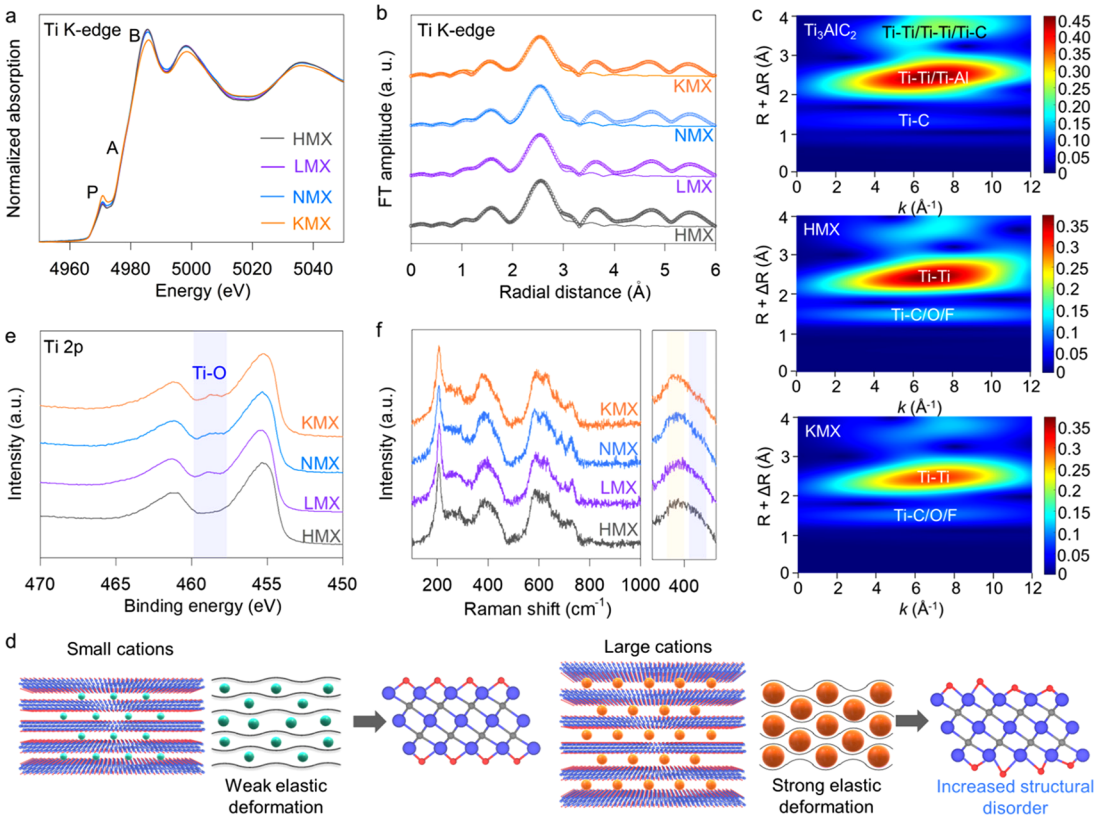

Figure 2. (a) Ti K-edge XANES, (b) Ti K-edge FT-EXAFS, (c) wavelet transform-EXAFS, (d) schematic diagram of the MXene-nanoparticle assembly and nanoparticle-caused deformation of MXene sheets, (e) Ti 2p XPS, and (f) micro-Raman spectra of assembled MXene nanosheets.

https://doi.org/10.1021/acsnano.3c09640
ACS Nano 2024, 18, 6243−6255

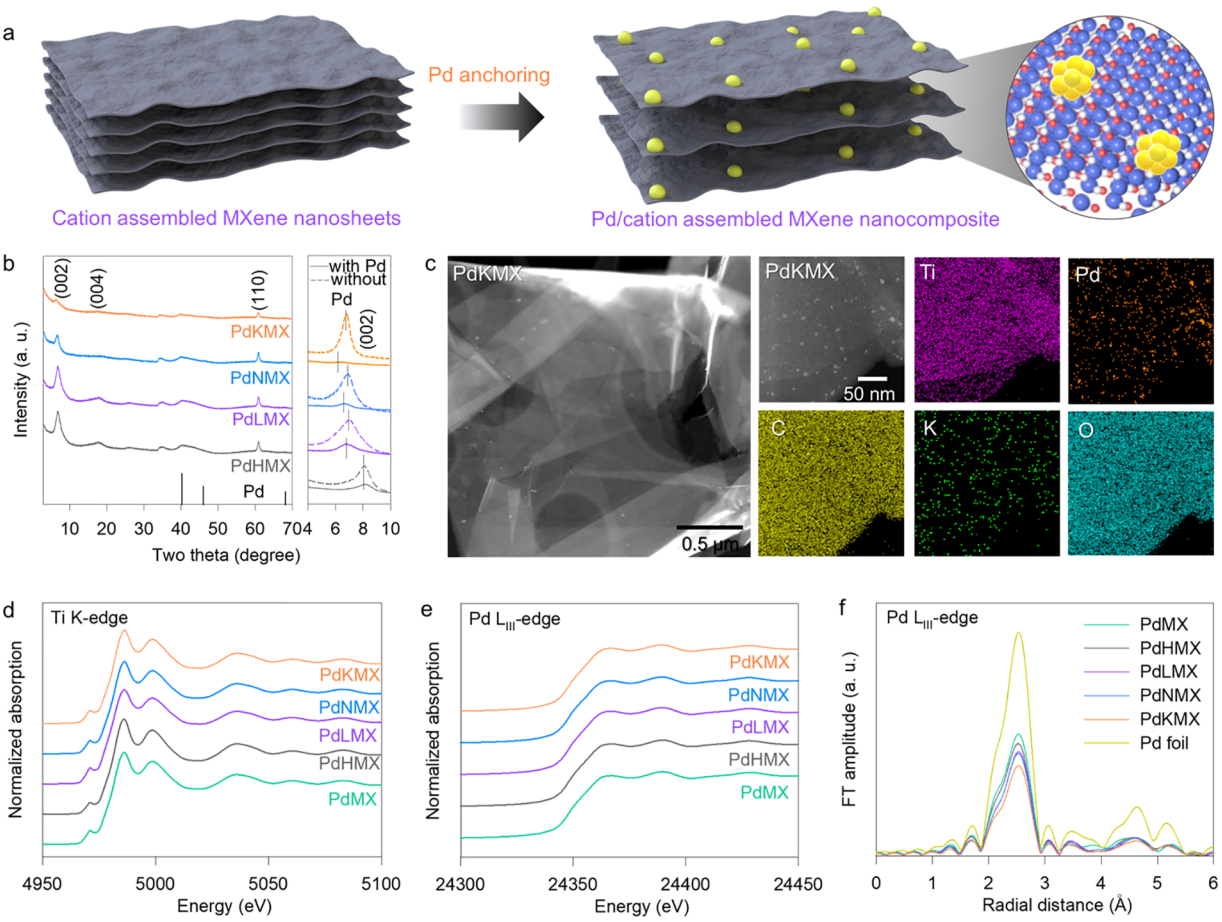

Figure 3. (a) Scheme for the immobilization of Pd nanoparticles on assembled MXene nanosheets. (b) Powder XRD, (c) HAADF-STEM and EDS-elemental maps, (d) Ti K-edge XANES, (e) Pd L_{III}-edge XANES, and (f) Pd L_{III}-edge FT-EXAFS of Pd−MXene nanohybrids.

assembly process. The greater stacking number of HMX compared to LMX and NMX can be attributed to an enhanced chemical interaction between the protons and oxygen on MXene nanosheets.[21] A crucial role of the electrostatic interaction and hydration layers in controlling the thickness of assembled MXene nanosheets was further corroborated by the thickening of the MXene nanosheets assembled with divalent alkaline earth metals such as Mg^{2+} and Ca^{2+} ions (Figure S3).[11] This is due to the higher charge densities and thinner hydration layers of these ions compared to the alkali metal ions (Tables S2 and S3). The uniform spatial distribution of Ti, C, and Na/K was demonstrated through elemental mapping analysis using energy-dispersive X-ray spectroscopy (EDS) (Figures 1d and S4), underscoring the uniform distribution of guest alkali metal ions between the $Ti_3C_2T_x$ nanosheets. Based on EDS results, the atomic ratios of Na/Ti and K/Ti were determined to be 0.024 and 0.034 in the NMX and KMX materials, respectively (Table S4). The porous nature of the MXene assemblies was verified using field-emission scanning electron microscopy (FE-SEM), see Figure 1e.

The significant effect of the guest type on the local atomic arrangement and electronic structure of assembled MXene nanosheets was verified by combined electronic and vibrational spectroscopy. As shown in Figure 2a, all assembled MXene nanosheets had similar Ti K-edge X-ray absorption near-edge structure (XANES) characteristics of the $Ti_3C_2T_x$ phase,[22] confirming that the MXene lattice is retained during the assembling process. As the guest ion size increases, the intensity of the pre-edge peak P related to the dipole-forbidden 1s → 3d transition increases.[23] Because this transition is partially allowed by structural distortion,[24] the enhancement of the peak P may be owing to the increase in local structural disorder, which followed the order of HMX < LMX < NMX < KMX. Simultaneously, the enlargement of the guest cations resulted in a decrease in the main-edge peaks A and B, which correspond to the dipole-allowed 1s → 4p transition,[25] confirming the enhanced structural disorder.

Furthermore, Ti K-edge extended X-ray absorption fine structure (EXAFS) analysis suggested a decrease in structural perfection with increasing intercalant ion size. As shown in Figure S5, all materials exhibited the typical Ti K-edge EXAFS oscillations of the $Ti_3C_2T_x$ phase, indicating that the MXene lattice was retained during self-assembly. A closer inspection revealed that the enlargement of guest ions caused a decrease in the amplitude of the EXAFS oscillation, confirming that the structural disordering was enhanced. Similarly, in Figure 2b, the typical Fourier transform (FT) characteristics of the MXene phase appeared at ∼1.7, ∼2.6, ∼3.1, and ∼3.7 Å in all the materials, corresponding to the Ti−C/O/F, Ti−Ti, Ti−Ti, and Ti−C bonding pairs, respectively.[26,27] The increase in guest size led to a decrease in the intensities of the FT peaks related to the Ti−C/O/F and Ti−Ti coordination shells, attesting to some enhancement of structural disorder. Based on the nonlinear least-squares fitting analysis results (Table S5), the coordination numbers of the Ti−C/O/F and Ti−Ti bonds

https://doi.org/10.1021/acsnano.3c09640
ACS Nano 2024, 18, 6243−6255

decreased with increasing guest ion size, verifying a decreased order with the lowering of coordination number and/or the increase of crystal vacancy. In addition, alkali metal-assembled MXene materials showed slightly larger Debye−Waller (σ^2) factors for the Ti−C/O/F bonding pair compared with proton-assembled HMX, reflecting the increase of structural disorder with an increase of *d*-spacing (Table S5).[27] This fitting result was further confirmed by Ti K-edge wavelet transform analysis, which showed lower intensities for the Ti−C/O/F and Ti−Ti bond contours of KMX than for those of HMX (Figure 2c). These XANES/EXAFS results provide strong evidence of the controllability of the ordering in exfoliated MXene nanosheets by tuning the guest size for self-assembly (Figure 2d).

The distinct influence of the guest size on the surface properties of the assembled MXene nanosheets was also confirmed by the surface-sensitive X-ray photoelectron spectra (XPS) technique. As shown in Figure 2e, the enlargement of guest species increased the spectral weight of the TiO_2 component (458.8 eV), indicating the enhanced oxygenation of the surface of MXene. The observed XPS results could be interpreted as increased oxidation of the MXene surface with an increase in interlayer spacing in the presence of ions with larger solvation shells.[28] This result was further confirmed by micro-Raman analysis. As shown in Figure 2f, all the materials exhibited the typical Raman characteristics of the MXene phase, such as the out-of-plane A_{1g} vibrations of Ti, C, and surface groups at ∼200 cm^{-1}, the in-plane E_g vibrations of surface groups attached to Ti atoms at ∼230−470 cm^{-1} (i.e., the T_x region), the in-plane and out-of-plane vibrations of C atoms at ∼500−670 cm^{-1} (i.e., the C region), and the out-of-plane A_{1g} vibrations of C atoms at ∼730 cm^{-1}.[29,30] The increase in alkali metal cations enhanced the spectral weight of the in-plane E_g phonon line of Ti−O bonds at ∼230 cm^{-1}, supporting the increase in oxygenated titanium species due to the oxidation of Ti_3C_2. This may be due to enhanced surface accessibility with increased ion size. Controlled mild surface oxidation has been shown to minimize the restacking of MXene sheets and improve accessibility of the interlayer space.[31]

The produced porous MXene particles assembled using various cations were used as catalyst supports for Pd. As shown in Figure 3a, the anchoring of Pd nanoparticles was achieved by reacting the assembled MXene nanosheets with an aqueous $PdCl_2$ solution (2.0 wt % Pd) at 25 °C. The resulting Pd-anchored assembled MXene (Pd−MXene) nanohybrids are denoted as PdHMX, PdLMX, PdNMX, and PdKMX. Because the standard reduction potential of Pd^{2+}/Pd is higher than that of Ti species in MXene, the redox reaction could occur between the $PdCl_2$ precursor and MXene nanosheets. As reported previously, a mixing of $Pd^{2+}Cl_2$ with MXene induced the adsorption of the metal precursors on the surface groups of MXene, triggering the spontaneous galvanic replacement between Pd^{2+} and reductive Ti species and thus the surface anchoring of Pd^0 nanoparticles on MXene nanosheets.[32,33]

According to powder XRD analysis (Figure 3b), all Pd−MXene nanohybrids showed peaks related to the MXene phase but no Pd-related Bragg reflections, indicating that the Pd species are well-dispersed on the MXene substrate. Although the spectrum of PdHMX exhibited a negligible shift in MXene-related Bragg reflections compared to that of pristine HMX, the spectrum of the MXene nanosheets assembled with alkali metal ions showed a significant shift in the (*00l*) reflections in the lower angle region after Pd nanoparticle immobilization, indicating expansion of the interlayer spacing. As shown in Figure 3a, the significant expansion upon self-assembly with K^+ ions suggests that some Pd nanoparticles were confined between the MXene layers of the KMX material. This finding emphasizes that self-assembly with alkali metal ions endows assembled MXene materials with high layer flexibility to accommodate Pd nanoparticles in their interlayer regions and on their surfaces. This is in contrast to the PdHMX material, which exhibits an insignificant change in the interlayer distance owing to the smaller interlayer spacing of HMX that prevents the intercalation of Pd species. In addition to the peak shift, all the nanohybrids exhibited a significant intensity decrease in the (*00l*) reflections after Pd anchoring, indicating the enhancement of stacking faults and/or the thinning of lamella thickness. Although KMX showed a somewhat larger stacking thickness than those of the other homologues (Figure 1b), this material experienced a much more drastic decrease of the (*00l*) reflection caused by Pd anchoring, indicating that the expanded interlayer spacing and weakened interlayer interaction in KMX promote the delamination into fewer layers in lamellae, as schematically shown in Figure 3a. The decrease in stacking layer number upon Pd anchoring was supposed to increase the surface area, which may be advantageous for improving the catalytic performance of the immobilized Pd nanoparticles. The significant increase of gas-accessible surface area from 16.8 $m^2\ g^{-1}$ for KMX to 30.1 $m^2\ g^{-1}$ for PdKMX upon Pd anchoring was verified by N_2 adsorption−desorption isotherm measurements (Figure S6). This contrasts with the less prominent increase in surface area for HMX upon Pd anchoring (23.2 $m^2\ g^{-1}$ → 29.7 $m^2\ g^{-1}$).

The successful immobilization of Pd nanoparticles was confirmed through high-angle annular dark-field scanning transmission electron microscopy (HAADF-STEM) analysis (Figure 3c). All Pd−MXene nanohybrids exhibited well-dispersed metal nanoparticles with a small diameter of several nanometers, firmly stabilized on the surface of the MXene nanosheets. This could be ascribed to the robust anchoring of Pd nanoparticles on the assembled MXene nanosheets with enhanced surface accessibility. As presented in Figure S7, cross-sectional HAADF-STEM measurements for PdKMX provided convincing proof for the intercalation of Pd nanoparticles between the interlayer-expanded KMX layers. In contrast, PdHMX showed no incorporation of Pd nanoparticles between the HMX layers due to the dense stacking of MXene nanosheets, as suggested by the XRD results. The FE-SEM analysis revealed a consistent porous stacking structure composed of highly anisotropic 2D nanosheets for all nanohybrids (Figure S8). EDS−elemental mapping analysis provided compelling evidence for the homogeneous anchoring of Pd nanoparticles on the MXene nanosheets by demonstrating the uniform presence of Pd, Ti, C, K, and O throughout the samples (see Figure 3c). The incorporation of the Pd nanoparticles into the assembled MXene nanosheets was further confirmed by inductively coupled plasma−optical emission spectrometer (ICP−OES) measurements, which showed similar Pd contents of ∼0.99−1.10% for all materials under investigation.

We conducted Ti K-edge and Pd L_{III}-edge XANES and EXAFS analyses to investigate the chemical bonding characteristics of the immobilized Pd species in the assembled MXene nanohybrids. Ti K-edge XANES analysis (Figure 3d) revealed that all Pd−MXene nanohybrids exhibited Ti K-edge features

https://doi.org/10.1021/acsnano.3c09640
ACS Nano 2024, 18, 6243−6255

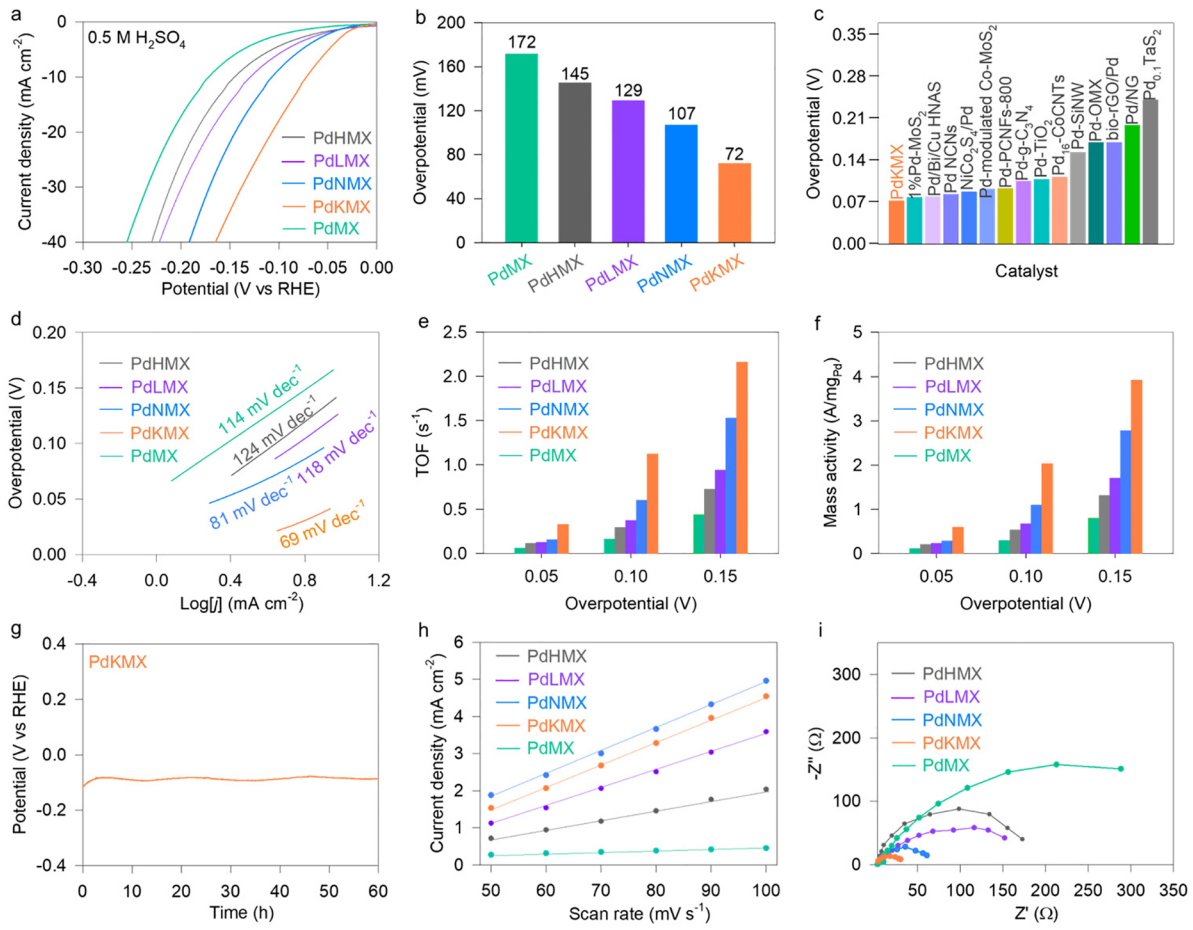

Figure 4. (a) LSV curves for HER in 0.5 M H_2SO_4 electrolyte, (b) overpotentials at 10 mA cm^{-2}, (c) comparison plot of HER overpotentials of Pd-based electrocatalysts, (d) Tafel plots, (e) TOF, (f) mass activity, (g) chronopotentiometry curve, (h) plot of the difference in current density vs scan rate, and (i) EIS data of Pd−MXene.

that were approximately identical to those of the MXene nanosheets, confirming the preservation of the MXene structure upon Pd anchoring. As shown in Figure 3e, Pd L_{III}-edge XANES spectra displayed distinctive features characteristic of zero-valent Pd metal species for all Pd−MXene nanohybrids.[34] These spectral features were easily distinguishable from those of the $Pd^{2+}Cl_2$ reference, providing strong evidence for the formation of Pd metal nanoparticles. In the Pd L_{III}-edge EXAFS spectra (Figure 3f), all Pd−MXene nanohybrids exhibited a prominent FT peak assigned to the Pd−Pd pair at ∼2−3 Å.[34] This FT peak confirmed the stabilization of the Pd metal nanoparticles. Furthermore, the intensity of this FT peak gradually decreased with increasing number of alkali metal ions in the assembled MXene nanosheets, indicating a decrease in the structural coherence of the immobilized Pd nanoparticles. As summarized in Figure S9 and Table S6, nonlinear least-squares fitting analysis confirmed the stabilization of the Pd nanoparticles with a reduced coordination number in the range of approximately 5.96 to 6.50. The decreased coordination numbers for the Pd−Pd bonding pairs underscore the effective stabilization of small Pd nanoparticles between the MXene nanosheets. The decrease in the coordination number of the Pd−Pd bond with increasing guest size provides another convincing support for the enhanced interfacial interaction with the Pd nanoparticles inserted between the MXene nanosheets when the spacing is expanded.

All assembled Pd−MXene nanohybrids were employed as electrocatalysts for the hydrogen evolution reaction (HER) in a 0.5 M H_2SO_4 electrolyte at a scan rate of 5 mV s^{-1} to investigate the validity of MXene nanosheets as a hybridization matrix for Pd nanoparticles. As a control sample, Pd-anchoring was performed on the exfoliated MXene nanosheets (i.e., PdMX) by reacting the $PdCl_2$ precursor with freeze-dried MXene nanosheets under identical synthetic conditions to validate the benefit of immobilization on the assembled MXene nanosheets. Linear sweep voltammetry (LSV) curves (Figure 4a) demonstrated that all the Pd-anchored assembled MXene nanohybrids exhibited higher electrocatalytic activity than PdMX, indicating the merit of immobilization on the assembled MXene nanosheets. Among the Pd−MXene nanohybrids, PdKMX demonstrated the highest HER performance, with an overpotential of 72 mV at 10 mA cm^{-2}. This result highlights the enhanced electrocatalytic performance of the anchored Pd nanoparticles on KMX (Figure 4b). Furthermore, the HER electrocatalytic performance of PdKMX surpassed that of a commercial 20 wt % Pd/C catalyst,[35] Moreover, the observed HER performance of PdKMX was comparable or even superior to recently reported excellent data for Pd nanoparticle-based HER electrocatalysts (Table S7, Figure 4c).[35−48] This comparison highlights the significance of surface accessibility and stacking control in assembled MXene nanosheets for developing high-performance hybrid electrocatalysts. Additionally, the effect of Pd

https://doi.org/10.1021/acsnano.3c09640
ACS Nano 2024, 18, 6243−6255

concentration on the electrocatalyst performance was examined by preparing PdKMX materials with different Pd contents. As presented in Figure S10, the PdKMX prepared with a 2 wt % $PdCl_2$ precursor was found to deliver better HER activity than the other homologues with smaller or larger amounts of $PdCl_2$ precursor, confirming the optimal Pd composition for this material.

The role of KMX as a hybridization matrix in enhancing the HER kinetics was further confirmed through Tafel slope measurements (Figure 4d), demonstrating the smallest Tafel slope for PdKMX. In terms of Pd species content, the turnover frequency (TOF) of the PdKMX nanohybrid was estimated to be 1.122 s^{-1} (at an overpotential of 100 mV), surpassing the TOFs of the other homologues (0.293 s^{-1} for PdHMX, 0.371 s^{-1} for PdLMX, 0.602 s^{-1} for PdNMX, and 0.159 s^{-1} for PdMX) (Figure 4e). This outcome provides further evidence for the beneficial role of KMX nanosheets as an immobilization matrix for hybrid electrocatalysts. Notably, the TOF of PdKMX was greater than those of recently reported Pd nanoparticle-based HER electrocatalysts (Table S7), emphasizing the exceptional efficacy of this material. The excellent HER performance of PdKMX was further confirmed by its superior mass activity compared to those of other homologues (Figure 4f). Additionally, chronopotentiometry measurements conducted at a current density of 10 mA cm^{-2} (Figure 4g) demonstrated that PdKMX experienced only a weak potential decay of 1.2% after the stability test for 60 h. This performance was better than those of the other homologues, indicating the outstanding durability of PdKMX. The high efficacy of KMX in enhancing the electrochemical activity of anchored Pd nanoparticles was further verified by measuring the electrochemically active surface areas (ECSAs) of the Pd−MXene nanohybrids. The plot of difference in current density versus scan rate (Figure 4h) showed the electrochemical double layer capacitances (C_{dl}) of PdHMX, PdLMX, PdNMX, and PdKMX to be 26.66, 49.39, 60.55, and 62.29 mF cm^{-2}, respectively, demonstrating the increase in ECSA in the following order: PdHMX < PdLMX < PdNMX < PdKMX. The distinct variations in the charge-transfer behavior of the Pd−MXene nanohybrids with different guest species were confirmed through electrochemical impedance spectroscopy (EIS). Figure 4i shows that all nanohybrids exhibited nearly identical spectral features with a semicircle in the mid-to-high-frequency region. The diameter of the semicircle decreased with increasing size of guest ions, indicating the improvement of interfacial charge transfer.[49] The fitting analysis using an equivalent circuit evaluated the charge transfer resistance (R_{ct}) for PdKMX to be 34.8 Ω, which is smaller than the R_{ct} values of the other homologues (193.0 Ω for PdHMX, 182.0 Ω for PdLMX, 76.4 Ω for PdNMX, and 459.0 Ω for PdMX).

The improved HER performance of PdKMX could be ascribed to the optimization of the assembly structure in KMX with expanded *d*-spacing. As evidenced by cross-sectional HAADF-STEM analysis (Figure S7), the larger *d*-spacing of KMX allowed intercalation of the Pd nanoparticles into the interlayer space of MXene layers, which is in stark contrast to the case of PdHMX. Such encapsulation of Pd nanoparticles between MXene layers was considered to be effective in achieving the strong electronic coupling between Pd nanoparticles and the conductive MXene matrix through intimate contact at the nanoscale. Additionally, the larger *d*-spacing of KMX could facilitate the delamination of MXene layers during Pd anchoring, as found by power XRD results (Figure 3b). As evident from the N_2 adsorption−desorption isotherm measurements (Figure S6), the depression of the stacking number following Pd anchoring led to a significant expansion of the surface area and thus the increase in the ECSA. The largest ECSA of PdKMX made an important contribution to the highest HER activity of this material. In addition to the increase in *d*-spacing, as found by Ti K-edge EXAFS analysis, the assembly with K^+ ions induced a greater structural disorder and lower coordination numbers for Ti−C/O bonds than the other homologues (i.e., HMX, LMX, and NMX), revealing the occurrence of amorphization and/or decreased coordination in MXene nanosheets. As the increase in structural disorder degraded the overlaps between Ti 3d and O/C 2p orbitals inside the MXene lattice, the O/C 2p orbitals in the disordered MXene nanosheets have an extra capability to effectively induce the additional orbital overlaps with the anchored Pd nanoparticles.[5] Besides, the lowering in coordination number in KMX helped enhance the chemical interaction with Pd nanoparticles, because the decreased coordination on the surface of MXene nanosheets could provide more space to facilitate the interfacial coordination bonding between MXene and Pd nanoparticles. Both factors of amorphization and decreased coordination caused by the assembly with K^+ ions resulted in the reinforcement of chemical interaction between Pd nanoparticles and conductive MXene nanosheets, leading to the improvement of the electrical conductivity of the PdKMX material. The resulting promotion of the interfacial charge transport property made a significant contribution to the excellent HER performance of the PdKMX nanohybrid. In summary, the benefits of self-assembly with K^+ ions in optimizing the HER activity of immobilized Pd nanoparticles could be attributed to the intercalation of Pd nanoparticles and the increase of structural disorder in MXene nanosheets, inducing effective chemical interaction between Pd nanoparticles and MXene nanosheets and subsequently enhancing interfacial electronic coupling with the conductive MXene substrate.

The pivotal roles of the assembly structure and Pd anchoring site in MXene nanosheets in optimizing the electrocatalyst performance were further verified by synthesizing the greatly-interlayer-expanded MXene material via assembly with bulky tetrahexylammonium (THA^+) cations (The obtained material is denoted as THAMX). The resulting material was also employed as a hybridization matrix for Pd nanoparticles, yielding PdTHAMX. As plotted in Figure S11a, assembling with THA^+ ions caused a much greater lattice expansion of MXene compared with KMX. In contrast to PdKMX, the PdTHAMX material showed a slight high-angle shift and a weak depression of the (*002*) peak upon Pd anchoring, indicating no occurrence of the intercalation of Pd nanoparticles and inefficient delamination of MXene nanosheets. No intercalation of Pd nanoparticles in this PdTHAMX material was cross-confirmed by cross-sectional HAADF-STEM analysis (Figure S11b). The presence of hydrophobic organic cations would prevent the intercalation of Pd nanoparticles in the interlayer space of the MXene layers. The obtained PdTHAMX with interlayer organic cations was examined as an HER electrocatalyst. As depicted in Figure S11c, the PdTHAMX material delivered a notably lower electrocatalytic activity with a larger overpotential than that of PdKMX, indicating that the assembling with organic cations showed inferior efficiency in improving the electrocatalyst performance of MXene. As presented in Figure S11d,

https://doi.org/10.1021/acsnano.3c09640
ACS Nano 2024, 18, 6243−6255

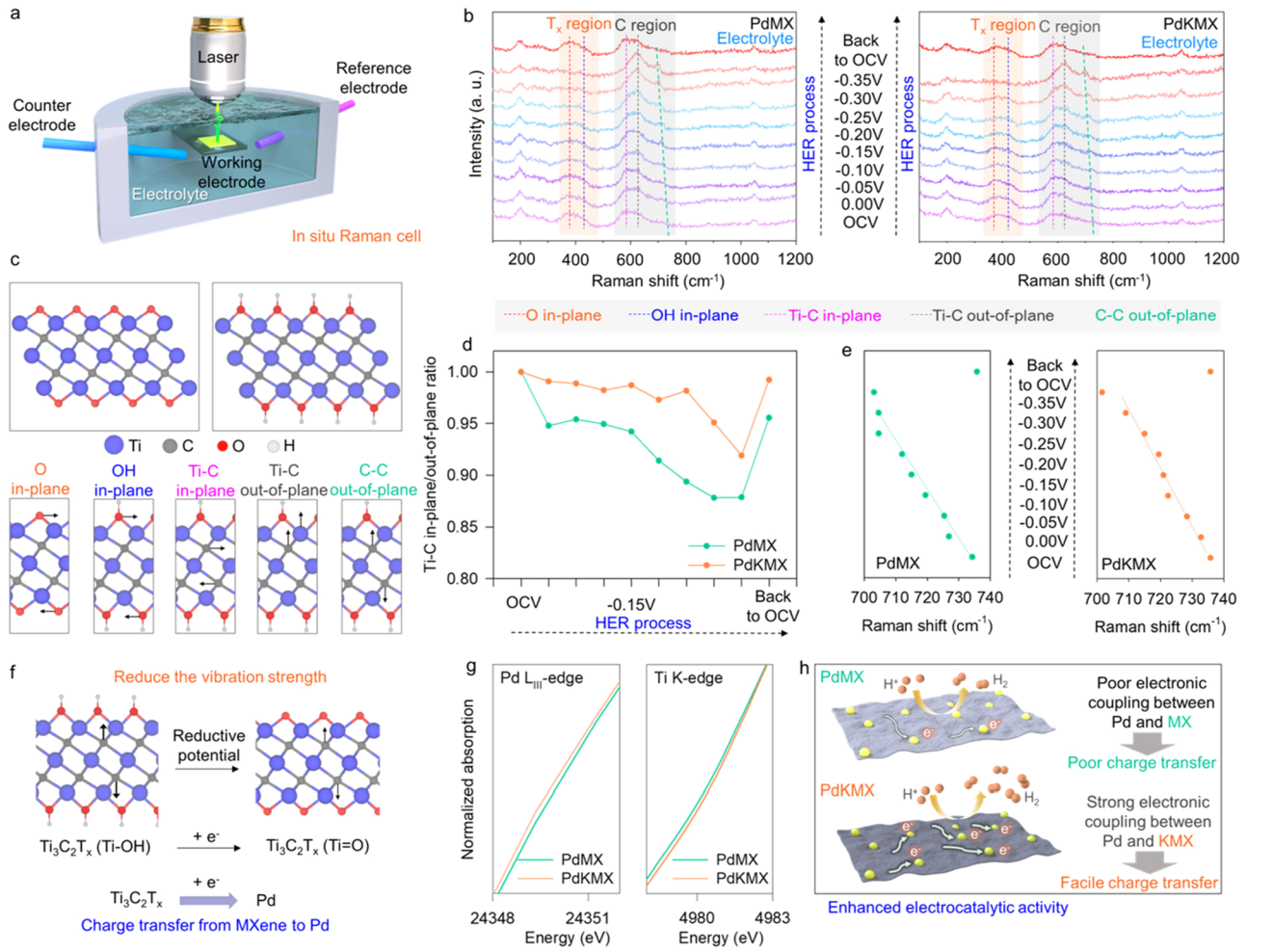

Figure 5. (a) Experimental setup for *in situ* Raman spectroscopy studies. (b) *In situ* Raman spectra for PdKMX and PdMX and (c) vibrational modes of the MXene lattice. (d) The plot of the in-plane/out-of-plane Ti−C peak ratio and (e) plot of A_{1g}(C) position as a function of applied potential. (f) Scheme for the effect of hydroxylation on A_{1g}(C) position. (g) Pd L_{III}-edge and Ti K-edge XANES spectra of PdKMX and PdMX. (h) Scheme for the electron transfer between the substrate and Pd species.

PdTHAMX possessed a smaller ECSA than that of PdKMX, reflecting the lower electrochemical activity of the former. The inferior electrocatalyst functionality of PdTHAMX could be attributed to no intercalation of Pd nanoparticles between the MXene nanosheets as well as negligible delamination of MXene layers. These findings provided another convincing evidence for the importance of Pd intercalation and MXene assembly structure in exploring efficient electrocatalysts.

To further confirm the profound influence of the binding site of Pd nanoparticles on electrocatalytic activity, unexfoliated MXene material was also prepared by the acid etching of pristine MAX material without a further exfoliation process and then employed as a hybridization matrix for the Pd nanoparticles (The obtained materials are denoted as unexfoliated MX and Pd−unexfoliated MX, respectively). Since the MXene layers in this material were densely packed, Pd nanoparticles could not be intercalated into the interlayer space but were stabilized only on the surface of the material. The uniform deposition of Pd nanoparticles on the surface of the unexfoliated MXene material was confirmed by EDS−elemental mapping analysis; see Figure S12a. According to the LSV measurements (Figure S12b), this Pd−unexfoliated MX material showed much weaker HER activity than PdKMX with a large overpotential, indicating the inferior performance of the unexfoliated MXene material as a hybridization matrix for Pd nanoparticles. As plotted in Figure S12c and S12d, the ECSA of Pd−unexfoliated MX was found to be much smaller than that of PdKMX, whereas the charge transport resistance of Pd−unexfoliated MX was greater than that of PdKMX, indicating that the unexfoliated MXene material led to fewer electrochemical active sites and slower charge transfer kinetics. This result provided additional support for the importance of Pd intercalation in improving the electrocatalyst performance and electrochemical activity of Pd nanoparticles.

To verify the usefulness of assembly structure control in optimizing the electrocatalyst performance of metal species immobilized on MXene nanosheets, the Ru nanoparticles were anchored on HMX and KMX materials (The obtained materials are denoted as RuHMX and RuKMX, respectively). As shown in Figure S13a, the KMX showed a significant low-angle shift and intensity depression of MXene-related XRD peaks upon Ru anchoring, similar to the observations for Pd-anchored KMX. According to the LSV measurements (Figure S13b), the Ru-anchored KMX material delivered a higher HER electrocatalyst activity with a lower overpotential than that of RuHMX, verifying the superior performance of KMX as a hybridization matrix. As plotted in Figure S13c, the EIS measurements clearly demonstrated that RuKMX displayed

https://doi.org/10.1021/acsnano.3c09640
ACS Nano 2024, 18, 6243−6255

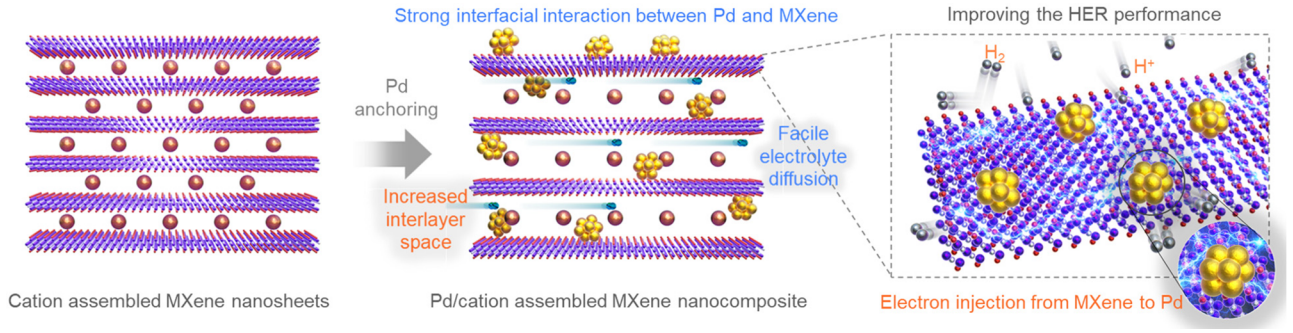

Figure 6. Schematic showing intercalation of metal ions, formation of Pd nanoparticles between MXene nanosheets, and stacking control during assembly of MXene nanosheets with Pd for improving the electrode functionality.

better charge transport kinetics than RuHMX. This finding emphasized the validity of the lattice engineering strategy in optimizing the performance of MXene-based hybrid catalyst materials.

In situ Raman spectroscopy measurements were performed on PdKMX and PdMX to study the origin of the enhanced HER activity of the Pd nanoparticles immobilized on K^+-intercalated MXene nanosheets (i.e., KMX) (Figure 5a). As illustrated in Figure 5b, both materials displayed typical peaks of the MXene phase (Figure 5c).[29] Increasing the negative potential to −0.35 V induced distinct spectral changes in both PdKMX and PdMX materials, including the depression of the in-plane Ti−C peak, enhancement of the out-of-plane Ti−C peak, and gradual red-shift of the A_{1g}(C) peak. The subsequent decrease in the applied potential to the OCV restored the original Raman features, demonstrating the reversibility of the electrochemical processes, such as double-layer formation and surface redox (Figure 5b).[23]

The in-plane/out-of-plane Ti−C peak ratio decreased with a gradual increase in the reductive potential (Figure 5d). This observation is consistent with the hydroxylation of the MXene lattice through the surface attachment of protons, which is known to lower the in-plane/out-of-plane Ti−C peak ratio.[29] The slower and weaker depression of this ratio in PdKMX compared to PdMX upon increasing the reductive potential strongly suggests that Pd anchoring on the K^+-intercalated KMX substrate retards proton attachment and results in the hydroxylation of the MXene layers concerning the freeze-dried MXene nanosheets (i.e., MX). The retardation of the hydroxylation of the MXene layer in PdKMX was further confirmed by the correlation plot of the A_{1g}(C) peak versus the potential (Figure 5e). PdKMX exhibited slower shifts of this peak with increasing negative potential than PdMX. It was documented that the A_{1g}(C) peaks at ∼684, ∼708, and ∼730 cm^{-1} correspond to −OH termination, mixed −O(OH) termination coverage, and −O(OH) termination, respectively.[50,51] Thus, the red-shift of this peak during the HER process indicates a proton attachment to the oxygen terminal groups in the MXene lattice, weakening Ti−C bonds due to forming −OH terminal groups (Figure 5f).[51,52] Hence, the slower shift of the A_{1g}(C) peak in PdKMX compared to PdMX confirms that the anchoring of Pd nanoparticles on the assembled KMX materials prevents the effective attachment of protons to the surface of the MXene nanosheets. *In situ* Raman measurement was also performed for the Pd−unexfoliated MX material during the electrocatalytic HER process. As presented in Figure S14, this material did not display any distinct spectral changes in the phonon lines during the HER process. This finding clearly substantiated that the stabilization of Pd nanoparticles in the interlayer space of MXene played a crucial role in improving the electrocatalytic activity of the Pd-anchored MXene nanohybrid.

To understand the benefits of self-assembly with K^+ ions in enhancing the interfacial electronic coupling between Pd nanoparticles and MXene nanosheets, O 1s XPS analysis was performed for PdKMX and PdMX. As shown in Figure S15, PdKMX showed a distinct high-energy shoulder in the O 1s peak corresponding to the surface oxygen groups in MXene interacting with Pd nanoparticles. Since the interfacial coordination bonding between MXene and Pd resulted in electron transfer from surface oxygen in MXene nanosheets to Pd nanoparticles, the observed high-energy shoulder peak could be interpreted as a result of effective interaction between MXene and Pd nanoparticles in PdKMX. Conversely, this shoulder peak appeared much weaker for PdMX, indicating much weaker interfacial interaction in this material compared with PdKMX. Additionally, the enhanced chemical interaction between MXene and Pd in PdKMX was further evidenced by the Pd L_{III}-edge and Ti K-edge XANES analyses. Figure 5g shows that PdKMX exhibits a lower Pd L_{III}-edge energy and a higher Ti K-edge energy than PdMX, indicating efficient interfacial interaction and resulting accumulation of electron density in the Pd nanoparticles of PdKMX (Figure 5h). These findings provide additional compelling evidence for the superior role of KMX in enhancing the interfacial electron injection from MXene to the Pd nanoparticles over MX. The charge redistribution in PdKMX promotes the predominant attachment of protons to the surface of the Pd nanoparticles, which is more efficient than that in PdMX. However, proton anchoring on the MXene nanosheet in PdKMX was inhibited owing to the accompanying depletion of electron density in the MXene nanosheet. In summary, the *in situ* Raman spectroscopy results reveal that the disordered, accessible, and reactive surface of the KMX substrate provides anchoring sites for Pd nanoparticles, facilitating electron injection from the MXene nanosheets to the Pd nanoparticles. The resulting activation of the Pd nanoparticles anchored on the KMX substrate is responsible for the improved HER functionality of PdKMX.

As illustrated in Figure 6, several factors are expected to contribute to the beneficial role of the KMX nanosheet as a hybridization matrix for improving the electrocatalytic activity of Pd nanoparticles. (1) Enhanced activation of Pd nanoparticles in the HER of PdKMX can be accomplished by intercalation of Pd between MXene nanosheets and an increase of structural disorder in MXene nanosheets, achieving strong interfacial electronic coupling with the KMX nanosheets and

https://doi.org/10.1021/acsnano.3c09640
ACS Nano 2024, 18, 6243−6255

then efficiently increasing the electron density of the Pd nanoparticles. This enhanced activation of Pd nanoparticles in PdKMX facilitates the adsorption and activation of H* during HER. The increasing accessibility of interlayer spacing in MXene during assembly with bulky K^+ ions allowed access to Pd ions and the formation of nanoparticles at active surface sites. We assume that the presence of Pd on only the outer surface of MXene lamellae is primarily responsible for the inferior HER activity of PdMX. (2) The K^+-intercalated KMX material possessed higher structural flexibility, inducing expansion of MXene stacks upon Pd anchoring compared to the MX substrate. Such an open interlayer spacing promotes the diffusion of reactants and electrolytes in PdKMX, which improves its electrocatalyst performance. (3) Simultaneously, the anchoring of Pd nanoparticles led to thinner MXene lamellae, less restacking, and larger accessible surface of the assembled KMX layers, providing additional surface-active sites. Such flexibility in the stacking structure of alkali-metal-intercalated MXenes improves the catalytic activity of the immobilized Pd species by enhancing mass transport and surface reactivity.

CONCLUSIONS

This study developed a strategy to regulate the assembly of 2D MXene nanosheets into a porous, crumpled catalyst support through coagulation with various alkali metal ions. The self-assembly with guest cations led to significant disorder and widening of the interlayer spacing. Intercalation of Pd nanoparticles between MXene nanosheets produced high-performance electrocatalysts for HER. Among the investigated materials, the K^+-intercalated MXene nanosheets showed the highest efficiency in enhancing the HER performance of Pd nanoparticles, surpassing recently published Pd nanoparticle-based catalysts. The weakening of the interlayer interaction as a result of self-assembly with bulky K^+ ions enhanced the structural tunability of the assembled MXene nanosheets, increasing the interlayer spacing, decreasing the stacking of layers, and allowing intercalation of Pd nanoparticles between the $Ti_3C_2T_x$ layers. The resulting increase in the number of catalytically active sites and enhanced mass transport resulted in the improved electrocatalytic performance of K^+-intercalated MXene. It is also anticipated that the presence of surface active sites in the MXene layers assisted in anchoring the Pd nanoparticles and enhanced the interfacial electronic coupling. The resulting electron injection from MXene into the Pd nanoparticles further contributed to the outstanding HER activity of the Pd−KMX nanohybrid. Considering the fact that the hybridization with conductive nanosheets is regarded as one of the most effective methods to improve the electrocatalytic activity of diverse inorganic materials,[53,54] the soft-chemical lattice engineering strategy developed in this study offers an economically feasible method for developing high-performance MXene-based hybrid electrocatalysts. Furthermore, the proposed strategy provides a synthetic basis for optimizing the functionalities of MXene nanosheets for other applications, such as electrodes, sensors, and electromagnetic shields, which are sensitive to the interlayer spacing and packing of 2D sheets.

METHODS

Materials Preparation. MXene ($Ti_3C_2T_x$) nanosheets were prepared by exfoliating the pristine MAX phase (i.e., Ti_3AlC_2). Typically, 1 g of MAX powder was reacted with an etchant containing 12 mL of 12 M hydrochloric acid, 6 mL of deionized water, and 2 mL of 50 wt % hydrofluoric acid. The reaction was performed at 35 °C for 24 h to selectively etch the Al layer. Subsequently, the suspension was washed multiple times with deionized water to remove residual acid and byproducts. The multilayer MXene was stirred in 50 mL of a 0.5 M solution of LiCl for 24 h, and the resulting mixture was washed several times with deionized water to remove residual Li^+ ions. Then, the product was restored by centrifugation at 3500 rpm multiple times, yielding a dark supernatant suspension containing exfoliated MXene.[17] The negatively charged MXene nanosheets were assembled with alkali metal cations (Li^+, Na^+, and K^+) and protons. 150 mL of a 0.5 M solution of chloride salts of various cations was slowly added to 150 mL of the colloidal suspension of exfoliated MXene nanosheets, resulting in the immediate flocculation of MXene nanosheets. After the reaction, the precipitates were thoroughly washed with distilled water and collected through high-speed centrifugation at 10000 rpm. The assembled MXene nanosheets were reacted with an aqueous $PdCl_2$ solution (2.0 wt % Pd) at 25 °C under stirring to immobilize Pd nanoparticles on the surface of the assembled MXene nanosheets. After synthesis, the resulting Pd−MXene nanohybrid precipitates were collected by using high-speed centrifugation and then oven-dried.

Materials Characterization. The 2D morphology and surface charge of the exfoliated MXene nanosheets were characterized using AFM (Park System, NX-10) and zeta potential measurements (Malvern Zetasizer Nano ZS instrument, UK), respectively. Powder XRD analysis (Rigaku Ultima IV, Ni-filtered Cu Kα radiation) was performed to determine the crystal structures and stacking thicknesses of the assembled MXene nanosheets and Pd−MXene nanohybrids. The crystal morphologies and stacking structures of the materials were examined using TEM (JEOL JEM-ARM200F, NEOARM), operated at an accelerating voltage of 200 kV, and FE-SEM (JEOL JSM-7001F microscope). Elemental mapping using EDS was performed to determine the spatial distribution of the constituent elements. The evolution of the electronic configuration of the assembled MXene nanosheets and the chemical bonding nature of the immobilized Pd nanoparticles were investigated through XANES and EXAFS analyses at the Ti K-edge and Pd L_{III}-edge, respectively. All XANES/EXAFS data were measured at beamlines 8C and 10C at the Pohang Accelerator Laboratory (PAL) in Korea. The data were processed using a standard procedure.[26] XPS analysis was performed to probe the interfacial charge transfer between the MXene nanosheet and guest cation/Pd nanoparticles using an XPS machine (Thermo VG, UK, Al Kα). All XPS spectra were energy-calibrated with reference to the Au 4f XPS peak (BE = 84 eV). *In situ* micro-Raman analysis was conducted by using a Horiba LabRam Aramis instrument with an Ar-ion laser (λ = 514.5 nm) as the excitation source. ICP-OES data were measured with Agilent 5110 equipment. N_2 adsorption−desorption analysis was performed with BELSORP-miniX (MicrotracBEL). The HAADF-STEM image was collected with the help of focused ion beam (FIB) sampling using a JEM-ARM 200F instrument.

Electrocatalyst Activity Measurement. An ink of the active catalysts was prepared to evaluate the HER activity of the Pd−MXene nanohybrids using the following procedure. 1.6 mg of catalyst and 20 μL of 5 wt % Nafion solution were dispersed in a 380 μL mixed solution of Milli-Q water/isopropanol (5/5, v/v). The resulting suspension was subjected to ultrasonication for 1 h. The working electrode was prepared by dropwise adding the mixture onto a carbon paper electrode (0.5 cm × 0.5 cm, torr) with 50 μL drops of catalyst ink, followed by drying at 40 °C in the oven. A graphite rod and a saturated calomel electrode (SCE) were used as the counter and reference electrodes, respectively. N_2-saturated 0.5 M H_2SO_4 solution was used as the acidic electrolyte. All electrical potentials were converted with reference to the RHE potential. An IVIUM analyzer with a conventional three-electrode cell was used to assess the cyclic voltammetry (CV) and LSV data. The LSV curves were collected at a scan rate of 5 mV s^{-1}. The Tafel slopes were determined by plotting the overpotential (η) against log |j|. An IVIUM analyzer was used to measure the EIS data in the 1000 kHz−0.1 Hz frequency range. The

https://doi.org/10.1021/acsnano.3c09640
ACS Nano 2024, 18, 6243−6255

TOF values of the present materials were calculated based on the concentration of active sites using the follow equation:

$$TOF = \frac{Number\ of\ total\ hydrogen\ turnovers/cm^2\ of\ geometric\ area}{Number\ of\ active\ sites\ (catalysts)/cm^2\ of\ geometric\ area}$$

The active sites were estimated based on the hypothesis that all the Pd atoms in the Pd−MXene could act as active sites and were accessible to the electrolyte.

$$Number\ of\ active\ sites = \frac{x}{100}\frac{mg}{mg} \times y\frac{mg}{cm^2} \times \frac{1}{M}\frac{mmol}{mg} \times 6.02 \times 10^{20}\frac{sites}{mmol}$$

where x represents the Pd concentration which was determined from the ICP−OES result. y represents the working electrode area. The total number of H_2 turnovers was calculated from the current density.

$$Total\ number\ of\ hydrogen\ turnover = j\frac{mA}{cm^2} \times \frac{\frac{1C}{s}}{1000\ mA} \times \frac{1\ mol\ e^-}{96485.3C} \times \frac{1\ mol\ H_2}{2\ mol\ e^-} \times \frac{6.02 \times 10^{23}\ molecules\ H_2}{1\ mol\ H_2} = 3.12 \times 10^{15}\frac{\frac{H_2}{s}}{cm^2}\ per\ \frac{mA}{cm^2}$$

Therefore, the TOF of the Pd−MXene catalysts at different overpotentials was calculated as follows:

$$TOF = \frac{3.12 \times 10^{15}\frac{\frac{H_2}{s}}{cm^2} \times j\frac{mA}{cm^2}}{Number\ of\ active\ sites}$$

The mass activity was evaluated as follows:

$$Mass\ activity = \frac{j\frac{A}{cm^2}}{Mass\ (catalysts)/cm^2\ of\ geometric\ area}$$

ASSOCIATED CONTENT

Supporting Information

The Supporting Information is available free of charge at https://pubs.acs.org/doi/10.1021/acsnano.3c09640.

AFM, TEM, and zeta potential data of exfoliated MXene nanosheets. Thickness plots, XRD data, EDS-mapping data, k^3-weighted Ti K-edge EXAFS oscillations, and EXAFS fitting results of assembled MXene nanosheets. N_2 adsorption−desorption isotherm, cross-sectional HADDF-STEM image, FE-SEM, Pd L_{III}-edge EXAFS fitting data, LSV curves, EIS curves, ECSA, *in situ* Raman, and XPS of Pd-anchored assembled MXene nanohybrids. XRD data, LSV, and EIS data of Ru-anchored assembled MXene nanohybrids. Ionic radii and hydration shell radii of various cations, elemental content, EXAFS fitting results, and electrocatalytic activity comparison tables for Pd-based catalysts. (PDF)

AUTHOR INFORMATION

Corresponding Authors

Xiaoyan Jin − *Department of Materials Science and Engineering, Yonsei University, Seoul 03722, Republic of Korea*; Email: xyjin313@yonsei.ac.kr

Yury Gogotsi − *A. J. Drexel Nanomaterials Institute, and Department of Materials Science and Engineering, Drexel University, Philadelphia, Pennsylvania 19104, United States*; orcid.org/0000-0001-9423-4032; Email: gogotsi@drexel.edu

Seong-Ju Hwang − *Department of Materials Science and Engineering, Yonsei University, Seoul 03722, Republic of Korea*; orcid.org/0000-0003-0233-1826; Email: hwangsju@yonsei.ac.kr

Authors

Yiyang Sun − *Department of Materials Science and Engineering, Yonsei University, Seoul 03722, Republic of Korea*

Jihyeong Lee − *Department of Materials Science and Engineering, Yonsei University, Seoul 03722, Republic of Korea*

Nam Hee Kwon − *Department of Materials Science and Engineering, Yonsei University, Seoul 03722, Republic of Korea*; orcid.org/0000-0001-6730-0970

Joohyun Lim − *Department of Chemistry, Institute for Molecular Science and Fusion Technology, Multidimensional Genomics Research Center, Kangwon National University, Chuncheon, Gangwon 24341, Republic of Korea*; orcid.org/0000-0003-3880-2634

Complete contact information is available at: https://pubs.acs.org/10.1021/acsnano.3c09640

Notes

The authors declare no competing financial interest.

ACKNOWLEDGMENTS

This work was supported by a National Research Foundation of Korea (NRF) grant funded by the Korean government (MSIT) (RS-2023-00208355, No. NRF-2022M3H4A4086103). The research was supported by the Yonsei University Grab Grant 2021-22-0304. The experiments at PAL were supported in part by MOST and POSTECH. Y.G. was also supported by the US National Science Foundation grant CHE-2318105 and the NSF Center for MXenes Synthesis, Tunability and Reactivity (M-STAR).

REFERENCES

(1) VahidMohammadi, A.; Rosen, J.; Gogotsi, Y. The World of Two-Dimensional Carbides and Nitrides (MXenes). *Science* **2021**, *372*, 1165.

(2) Lim, K. R. G.; Shekhirev, M.; Wyatt, B. C.; Anasori, B.; Gogotsi, Y.; Seh, Z. W. Fundamentals of MXene Synthesis. *Nat. Synth.* **2022**, *1*, 601−614.

(3) Zhang, J.; Zhao, Y.; Guo, X.; Chen, C.; Dong, C.-L.; Liu, R.-S.; Han, C.-P.; Li, Y.; Gogotsi, Y.; Wang, G. Single Platinum Atoms Immobilized on an MXene as an Efficient Catalyst for the Hydrogen Evolution Reaction. *Nat. Catal.* **2018**, *1*, 985−992.

(4) Qu, X.; Guo, Y.; Xie, C.; Li, S.; Liu, Z.; Lei, B. Photoactivated MXene Nanosheets for Integrated Bone-Soft Tissue Therapy: Effect and Potential Mechanism. *ACS Nano* **2023**, *17*, 7229−7240.

(5) Jin, X.; Park, M.; Shin, S.-J.; Jo, Y.; Kim, M. G.; Kim, H.; Kang, Y.-M.; Hwang, S.-J. Synergistic Control of Structural Disorder and Surface Bonding Nature to Optimize the Functionality of Manganese Oxide as an Electrocatalyst and a Cathode for Li-O_2 Batteries. *Small* **2020**, *16*, 1903265.

(6) Ferrara, C.; Gentile, A.; Marchionna, S.; Quinzeni, I.; Fracchia, M.; Ghigna, P.; Pollastri, S.; Ritter, C.; Vanacore, G. M.; Ruffo, R. The Missing Piece: The Structure of the $Ti_3C_2T_x$ MXene and Its Behavior as Negative Electrode in Sodium Ion Batteries. *Nano Lett.* **2021**, *21*, 8290−8297.

(7) Guo, Y.; Wang, T.; Yang, Q.; Li, X.; Li, H.; Wang, Y.; Jiao, T.; Huang, Z.; Dong, B.; Zhang, W.; Fan, J.; Zhi, C. Highly Efficient

Electrochemical Reduction of Nitrogen to Ammonia on Surface Termination Modified $Ti_3C_2T_x$ MXene Nanosheets. *ACS Nano* **2020**, *14*, 9089−9097.
(8) VahidMohammadi, A.; Mojtabavi, M.; Caffrey, N. M.; Wanunu, M.; Beidaghi, M. Assembling 2D MXenes into Highly Stable Pseudocapacitive Electrodes with High Power and Energy Densities. *Adv. Mater.* **2019**, *31*, 1806931.
(9) Zhao, D.; Clites, M.; Ying, G.; Kota, S.; Wang, J.; Natu, V.; Wang, X.; Pomerantseva, E.; Cao, M.; Barsoum, M. W. Alkali-Induced Crumpling of $Ti_3C_2T_x$ (MXene) to Form 3D Porous Networks for Sodium Ion Storage. *Chem. Commun.* **2018**, *54*, 4533−4536.
(10) Li, K.; Liang, M.; Wang, H.; Wang, X.; Huang, Y.; Coelho, J.; Pinilla, S.; Zhang, Y.; Qi, F.; Nicolosi, V.; Xu, Y. 3D MXene Architectures for Efficient Energy Storage and Conversion. *Adv. Funct. Mater.* **2020**, *30*, 2000842.
(11) Kim, N.; Gu, T.-H.; Shin, D.; Jin, X.; Shin, H.; Kim, M. G.; Kim, H.; Hwang, S.-J. Lattice Engineering to Simultaneously Control the Defect/Stacking Structures of Layered Double Hydroxide Nanosheets to Optimize Their Energy Functionalities. *ACS Nano* **2021**, *15*, 8306−8318.
(12) Lim, J.; Jin, X.; Jo, Y. K.; Lee, S.; Hwang, S.-J. Kinetically Controlled Layer-by-Layer Stacking of Metal Oxide 2D Nanosheets. *Angew. Chem. Int. Ed.* **2017**, *129*, 7199−7202.
(13) Gu, T.-H.; Jin, X.; Park, S.-J.; Kim, M. G.; Hwang, S.-J. Molecular-Level Control of the Intersheet Distance and Electronic Coupling between 2D Semiconducting and Metallic Nanosheets: Establishing Design Rules for High-Performance Hybrid Photocatalysts. *Adv. Sci.* **2021**, *8*, 2004530.
(14) Kwon, N. H.; Shin, S.-J.; Jin, X.; Jung, Y.; Hwang, G.-S.; Kim, H.; Hwang, S.-J. Monolayered g-C_3N_4 Nanosheet as an Emerging Cationic Building Block for Bifunctional 2D Superlattice Hybrid Catalysts with Controlled Defect Structures. *Appl. Catal. B: Environ.* **2020**, *277*, 119191.
(15) Li, X.; Huang, Z.; Shuck, C. E.; Liang, G.; Gogotsi, Y.; Zhi, C. MXene Chemistry, Electrochemistry and Energy Storage Applications. *Nat. Rev. Chem.* **2022**, *6*, 389−404.
(16) Liu, A.; Liang, X.; Ren, X.; Guan, W.; Gao, M.; Yang, Y.; Yang, Q.; Gao, L.; Li, Y.; Ma, T. Recent Progress in MXene-Based Materials: Potential High-Performance Electrocatalysts. *Adv. Funct. Mater.* **2020**, *30*, 2003437.
(17) Shuck, C. E.; Ventura-Martinez, K.; Goad, A.; Uzun, S.; Shekhirev, M.; Gogotsi, Y. Safe Synthesis of MAX and MXene: Guidelines to Reduce Risk During Synthesis. *ACS Chem. Health Saf.* **2021**, *28*, 326−338.
(18) Gao, Q.; Sun, W.; Ilani-Kashkouli, P.; Tselev, A.; Kent, P. R. C.; Kabengi, N.; Naguib, M.; Alhabeb, M.; Tsai, W.-Y.; Baddorf, A. P.; Huang, J.; Jesse, S.; Gogotsi, Y.; Balke, N. Tracking Ion Intercalation into Layered Ti_3C_2 MXene Films across Length Scales. *Energy Environ. Sci.* **2020**, *13*, 2549−2558.
(19) Li, J.; Yuan, X.; Lin, C.; Yang, Y.; Xu, L.; Du, X.; Xie, J.; Lin, J.; Sun, J. Achieving High Pseudocapacitance of 2D Titanium Carbide (MXene) by Cation Intercalation and Surface Modification. *Adv. Energy Mater.* **2017**, *7*, 1602725.
(20) Gao, X.; Du, X.; Mathis, T. S.; Zhang, M.; Wang, X.; Shui, J.; Gogotsi, Y.; Xu, M. Maximizing Ion Accessibility in MXene-Knotted Carbon Nanotube Composite Electrodes for High-Rate Electrochemical Energy Storage. *Nat. Commun.* **2020**, *11*, 6160.
(21) Lounasvuori, M.; Sun, Y.; Mathis, T. S.; Puskar, L.; Schade, U.; Jiang, D.-E.; Gogotsi, Y.; Petit, T. Vibrational Signature of Hydrated Protons Confined in MXene Interlayers. *Nat. Commun.* **2023**, *14*, 1322.
(22) Magnuson, M.; Naslund, L.-A. Local Chemical Bonding and Structural Properties in Ti_3AlC_2 MAX phase and $Ti_3C_2T_x$ MXene Probed by Ti 1s X-Ray Absorption Spectroscopy. *Phys. Rev. Res.* **2020**, *2*, 033516.
(23) Lukatskaya, M. R.; Bak, S.-M.; Yu, X.; Yang, X.-Q.; Barsoum, M. W.; Gogotsi, Y. Probing the Mechanism of High Capacitance in 2D Titanium Carbide Using In Situ X-Ray Absorption Spectroscopy. *Adv. Energy Mater.* **2015**, *5*, 1500589.
(24) Jin, X.; Lee, T.; Tamakloe, W.; Patil, S. B.; Soon, A.; Kang, Y.-M.; Hwang, S.-J. In Situ Defect Engineering Route to Optimize the Cationic Redox Activity of Layered Double Hydroxide Nanosheet via Strong Electronic Coupling with Holey Substrate. *Adv. Sci.* **2022**, *9*, 2103368.
(25) Triana, C. A.; Araujo, C. M.; Ahuja, R.; Niklasson, G. A.; Edvinsson, T. Electronic Transitions Induced by Short-Range Structural Order in Amorphous TiO_2. *Phys. Rev. B* **2016**, *94*, 165129.
(26) Hou, T.; Luo, Q.; Li, Q.; Zu, H.; Cui, P.; Chen, S.; Lin, Y.; Chen, J.; Zheng, X.; Zhu, W.; Liang, S.; Yang, J.; Wang, L. Modulating Oxygen Coverage of $Ti_3C_2T_x$ MXenes to Boost Catalytic Activity for HCOOH Dehydrogenation. *Nat. Commun.* **2020**, *11*, 4251.
(27) Wang, X.; Bak, S.-M.; Han, M.; Shuck, C. E.; McHugh, C.; Li, K.; Li, J.; Tang, J.; Gogotsi, Y. Surface Redox Pseudocapacitance of Partially Oxidized Titanium Carbide MXene in Water-in-Salt Electrolyte. *ACS Energy Lett.* **2022**, *7*, 30−35.
(28) Natu, V.; Benchakar, M.; Canaff, C.; Habrioux, A.; Celerier, S.; Barsoum, M. W. A Critical Analysis of the X-Ray Photoelectron Spectra of $Ti_3C_2T_z$ MXenes. *Matter* **2021**, *4*, 1224−1251.
(29) Sarycheva, A.; Gogotsi, Y. Raman Spectroscopy Analysis of the Structure and Surface Chemistry of $Ti_3C_2T_x$ MXene. *Chem. Mater.* **2020**, *32*, 3480−3488.
(30) Soundiraraju, B.; George, B. K. Two-Dimensional Titanium Nitride (Ti_2N) MXene: Synthesis, Characterization, and Potential Application as Surface-Enhanced Raman Scattering Substrate. *ACS Nano* **2017**, *11*, 8892−8900.
(31) Tang, J.; Mathis, T. S.; Kurra, N.; Sarycheva, A.; Hatter, C.; Xiao, X.; Hedhili, M. N.; Jiang, Q.; Alshareef, H. N.; Xu, B.; Pan, F.; Gogotsi, Y. Tuning the Electrochemical Performance of Titanium Carbide MXene by Controllable In Situ Anodic Oxidation. *Angew. Chem. Int. Ed.* **2019**, *131*, 18013−18019.
(32) Wei, Z.; Zhao, Z.; Qiu, C.; Huang, S.; Yao, Z.; Wang, M.; Chen, Y.; Lin, Y.; Zhong, X.; Li, X.; Wang, J. Tripodal Pd Metallenes Mediated by Nb_2C MXenes for Boosting Alkynes Semihydrogenation. *Nat. Commun.* **2023**, *14*, 661.
(33) Ying, G.; Cao, X.; Wang, D.; Peng, Q.; Wang, G.; Chen, C. MXene (Ti_3C_2) Vacancy-Confined Single-Atom Catalyst for Efficient Functionalization of CO_2. *J. Am. Chem. Soc.* **2019**, *141*, 4086−4093.
(34) Liu, Z.; Huang, F.; Peng, M.; Chen, Y.; Cai, X.; Wang, L.; Hu, Z.; Wen, X.; Wang, N.; Xiao, D.; Jiang, H.; Sun, H.; Liu, H.; Ma, D. Tuning the Selectivity of Catalytic Nitriles Hydrogenation by Structure Regulation in Atomically Dispersed Pd Catalysts. *Nat. Commun.* **2021**, *12*, 6194.
(35) Luo, Z.; Ouyang, Y.; Zhang, H.; Xiao, M.; Ge, J.; Jiang, Z.; Wang, J.; Tang, D.; Cao, X.; Liu, C.; Xing, W. Chemically Activating MoS_2 via Spontaneous Atomic Palladium Interfacial Doping towards Efficient Hydrogen Evolution. *Nat. Commun.* **2018**, *9*, 2120.
(36) Zheng, L.; Zheng, S.; Wei, H.; Du, L.; Zhu, Z.; Chen, J.; Yang, D. Palladium/Bismuth/Copper Hierarchical Nano-Architectures for Efficient Hydrogen Evolution and Stable Hydrogen Detection. *ACS Appl. Mater. Interfaces* **2019**, *11*, 6248−6256.
(37) Zhang, X.-F.; Chen, Y.; Zhang, L.; Wang, A.-J.; Wu, L.-J.; Wang, Z.-G.; Feng, J.-J. Poly-L-Lysine Mediated Synthesis of Palladium Nanochain Networks and Nanodendrites as Highly Efficient Electrocatalysts for Formic Acid Oxidation and Hydrogen Evolution. *J. Colloid Interface Sci.* **2018**, *516*, 325−331.
(38) Sheng, G.; Chen, J.; Li, Y.; Ye, H.; Hu, Z.; Fu, X.-Z.; Sun, R.; Huang, W.; Wong, C.-P. Flowerlike $NiCo_2S_4$ Hollow Sub-Microspheres with Mesoporous Nanoshells Support Pd Nanoparticles for Enhanced Hydrogen Evolution Reaction Electrocatalysis in Both Acidic and Alkaline Conditions. *ACS Appl. Mater. Interfaces* **2018**, *10*, 22248−22256.
(39) Liu, S.; Zhou, L.; Zhang, W.; Jin, J.; Mu, X.; Zhang, S.; Chen, C.; Mu, S. Stabilizing Sulfur Vacancy Defects by Performing "Click" Chemistry of Ultrafine Palladium to Trigger a High-Efficiency Hydrogen Evolution of MoS_2. *Nanoscale* **2020**, *12*, 9943−9949.
(40) Li, L.; Gu, J.; Ye, Y.; Guo, J.; Zhao, J.; Zou, G. Effective Synergy Between Palladium Nanoparticles and Nitrogen-Doped Porous

https://doi.org/10.1021/acsnano.3c09640
ACS Nano 2024, 18, 6243−6255

Carbon Fiber for Hydrogen Evolution Reaction. *Electrochim. Acta* **2022**, *409*, 139959.
(41) Woldetinsay, M.; Soreta, T. R.; Maiyalagan, T.; Femi, O. E. Effect of Support Material on the Electrocatalytic Activity of Palladium Nanoparticle toward Hydrogen Evolution Reaction. *Mater. Res. Express* **2021**, *8*, 025501.
(42) Zeng, X.; Bai, Y.; Choi, S. M.; Tong, L.; Aleisa, R. M.; Li, Z.; Liu, X.; Yu, R.; Myung, N. V.; Yin, Y. Mesoporous TiO_2 Nanospheres Loaded with Highly Dispersed Pd Nanoparticles for pH-Universal Hydrogen Evolution Reaction. *Mater. Today Nano* **2019**, *6*, 100038.
(43) Huang, B.; Chen, L.; Wang, Y.; Ouyang, L.; Ye, J. Paragenesis of Palladium-Cobalt Nanoparticle in Nitrogen-Rich Carbon Nanotubes as a Bifunctional Electrocatalyst for Hydrogen-Evolution Reaction and Oxygen-Reduction Reaction. *Chem.—Eur. J.* **2017**, *23*, 7710−7718.
(44) Yin, K.; Cheng, Y.; Jiang, B.; Liao, F.; Shao, M. Palladium-Silicon Nanocomposites as a Stable Electrocatalyst for Hydrogen Evolution Reaction. *J. Colloid Interface Sci.* **2018**, *522*, 242−248.
(45) Kim, J. G.; Lee, B.; Pham, N. N. T.; Lee, S. G.; Pak, C. Relationship between Hydrogen Binding Energy and Activity for Hydrogen Evolution Reaction by Palladium Supported on Sulfur-Doped Ordered Mesoporous Carbon. *J. Ind. Eng. Chem.* **2020**, *89*, 361−367.
(46) Balun Kayan, D.; Turunç, E. Bio-Reduced GO/Pd Nanocomposite as an Efficient and Green Synthesized Catalyst for Hydrogen Evolution Reaction. *Int. J. Energy Res.* **2021**, *45*, 11146−11156.
(47) Guo, K.; Rowland, L. J.; Isherwood, L. H.; Glodan, G.; Baidak, A. Photon-Induced Synthesis of Ultrafine Metal Nanoparticles on Graphene as Electrocatalysts: Impact of Functionalization and Doping. *J. Mater. Chem. A* **2020**, *8*, 714−723.
(48) Wang, D.; Wang, X.; Lu, Y.; Song, C.; Pan, J.; Li, C.; Sui, M.; Zhao, W.; Huang, F. Atom-Scale Dispersed Palladium in a Conductive $Pd_{0.1}TaS_2$ Lattice with a Unique Electronic Structure for Efficient Hydrogen Evolution. *J. Mater. Chem. A* **2017**, *5*, 22618−22624.
(49) Jin, X.; Lee, K.-G.; Lee, T.; Lee, G.; Oh, S. M.; Soon, A.; Hwang, S.-J. Composition-Controlled Ultrathin Holey $TiO_{1-x}N_x$ Nanosheets as Powerful Hybridization Matrices for Highly Mass-Efficient Electrocatalysts. *Chem. Eng. J.* **2022**, *437*, 135415.
(50) Johnson, D.; Hansen, K.; Yoo, R.; Djire, A. Elucidating the Charge Storage Mechanism on Ti_3C_2 MXene through In Situ Raman Spectroelectrochemistry. *ChemElectroChem* **2022**, *9*, No. e202200555.
(51) Hu, T.; Wang, J.; Zhang, H.; Li, Z.; Hu, M.; Wang, X. Vibrational Properties of Ti_3C_2 and $Ti_3C_2T_2$ (T = O, F, OH) Monosheets by First-Principles Calculations: a Comparative Study. *Phys. Chem. Chem. Phys.* **2015**, *17*, 9997−10003.
(52) Zhang, L.; Su, W.; Huang, Y.; Li, H.; Fu, L.; Song, K.; Huang, X.; Yu, J.; Lin, C.-T. In Situ High-Pressure X-ray Diffraction and Raman Spectroscopy Study of $Ti_3C_2T_x$ MXene. *Nanoscale Res. Lett.* **2018**, *13*, 343.
(53) Jin, X.; Gu, T.-H.; Lee, K.-G.; Kim, M. J.; Islam, M. S.; Hwang, S.-J. Unique Advantages of 2D Inorganic Nanosheets in Exploring High-Performance Electrocatalysts: Synthesis, Application, and Perspective. *Coord. Chem. Rev.* **2020**, *415*, 213280.
(54) Jin, X.; Gu, T.-H.; Kwon, N. H.; Hwang, S.-J. Synergetic Advantages of Atomically-Coupled 2D Inorganic and Graphene Nanosheets as Versatile Building Blocks for Diverse Functional Nanohybrids. *Adv. Mater.* **2021**, *33*, 2005922.

https://doi.org/10.1021/acsnano.3c09640
ACS Nano 2024, 18, 6243−6255